



Published in final edited form as:

*J Control Release*. 2015 November 10; 217: 243–255. doi:10.1016/j.jconrel.2015.09.027.

## Hybrid nanoparticles improve targeting to inflammatory macrophages through phagocytic signals

Vaishali Bagalkot<sup>a</sup>, Marcus A. Badgeley<sup>b,1</sup>, Thomas Kampfrath<sup>b,2</sup>, Jeffrey A. Deiuiliis<sup>a,b</sup>, Sanjay Rajagopalan<sup>a,b</sup>, and Andrei Maiseyeu<sup>a,b,\*</sup>

<sup>a</sup>Division of Cardiovascular Medicine, Department of Medicine, University of Maryland, Baltimore, MD 21201, United States

<sup>b</sup>Davis Heart and Lung Research Institute, Ohio State University, Columbus, OH 43210, United States

### Abstract

Macrophages are innate immune cells with great phenotypic plasticity, which allows them to regulate an array of physiological processes such as host defense, tissue repair, and lipid/lipoprotein metabolism. In this proof-of-principle study, we report that macrophages of the M1 inflammatory phenotype can be selectively targeted by model hybrid lipid–latex (LiLa) nanoparticles bearing phagocytic signals. We demonstrate a simple and robust route to fabricate nanoparticles and then show their efficacy through imaging and drug delivery in inflammatory disease models of atherosclerosis and obesity. Self-assembled LiLa nanoparticles can be modified with a variety of hydrophobic entities such as drug cargos, signaling lipids, and imaging reporters resulting in sub-100 nm nano-particles with low polydispersities. The optimized theranostic LiLa formulation with gadolinium, fluorescein and “eat-me” phagocytic signals (Gd-FITC-LiLa) a) demonstrates high relaxivity that improves magnetic resonance imaging (MRI) sensitivity, b) encapsulates hydrophobic drugs at up to 60% by weight, and c) selectively targets inflammatory M1 macrophages concomitant with controlled release of the payload of anti-inflammatory drug. The mechanism and kinetics of the payload discharge appeared to be phospholipase A2 activity-dependent, as determined by means of intracellular Förster resonance energy transfer (FRET). In vivo, LiLa targets M1 macrophages in a mouse model of atherosclerosis, allowing noninvasive imaging of atherosclerotic plaque by MRI. In the context of obesity, LiLa particles were selectively deposited to M1 macrophages within inflamed adipose tissue, as demonstrated by single-photon intravital imaging in mice. Collectively, our results suggest that phagocytic signals

This is an open access article under the CC BY-NC-ND license (<http://creativecommons.org/licenses/by-nc-nd/4.0/>).

\*Corresponding author at: Division of Cardiovascular Medicine, Department of Medicine, University of Maryland, Baltimore, MD 21201, United States. ; Email: amaiseyeu@medicine.umaryland.edu (A. Maiseyeu).

<sup>1</sup>Present address: Icahn School of Medicine at Mount Sinai, York, NY 10029, United States.

<sup>2</sup>Present address: Santa Clara Valley Medical Center, San Jose, CA 95128, United States.

#### Author contributions

The manuscript was written through contributions of all authors. All authors have given approval to the final version of the manuscript.

#### Appendix A. Supplementary data

The following experimental materials and methods are included in the supporting information: materials, cell culture, Characterization, Cryo-TEM, Sensitized emission FRET, MR image analysis, pharmacokinetics and bio-distribution of Rosi-Gd-LiLa, liquid chromatography–mass spectrometry (LC–MS) analysis, total RNA extraction and quantitative real time PCR along with supplementary figures. Supplementary data to this article can be found online at <http://dx.doi.org/10.1016/j.jconrel.2015.09.027>.

can preferentially target inflammatory macrophages in experimental models of atherosclerosis and obesity, thus opening the possibility of future clinical applications that diagnose/treat these conditions. Tunable LiLa nanoparticles reported here can serve as a model theranostic platform with application in various types of imaging of the diseases such as cardiovascular disorders, obesity, and cancer where macrophages play a pathogenic role.

## Keywords

Theranostic nanoparticles; Inflammation; Atherosclerosis; Obesity; Magnetic resonance imaging; Intravital imaging

---

## 1. Introduction

Macrophages play a key role in initiating the inflammatory and immune responses that often becomes uncontrolled in diseases such as atherosclerosis, myocardial infarction, obesity, and cancer[1,2]. It has been shown that the number of inflammatory macrophages in atherosclerotic plaque correlates with plaque rupture[3]. In obesity, macrophages infiltrate the adipose tissue during weight gain and contribute to local and systemic inflammation eventually causing insulin resistance (IR) and type 2 diabetes mellitus. Medical imaging and therapeutic strategies that target tissue macrophages are intensively sought after due to their significant relevance in the etiology of cardiovascular and metabolic disease. Successful human translation of strategies honed in mouse models may allow for non-invasive detection of macrophage burden.

Nanoparticle-based probe delivery systems offer selective and effective detection of targeted cells. Nanoparticles labeled with imaging probes are often used for selective macrophage recognition. It is well established that circulating monocytes, splenic macrophages and disease-associated macrophages (for example in atherosclerotic plaque and tumor) rapidly engulf the nanoparticles by virtue of their intrinsic phagocytic ability[4]. It is clear that macrophage-targeted agents are well known, however, our ability to selectively image detrimental (“bad”) macrophages is very limited. New nanoparticle formulations are needed to overcome the hurdle of cell specificity manifested in the affinity of nanoparticles to multiple macrophage sub-types. For example, many currently available nanoparticles target both anti-inflammatory and pro-inflammatory macrophages and tend to be engulfed by other phagocytic cells such as dendritic cells and neutrophils. Time consuming screening studies are sometimes needed to obtain nanoparticle that target to specific cell population, or to devise the optimal physicochemical characteristics of the cell-targeted carrier such as size, charge, and shape[5]. Macrophage-targeted theranostics currently focus on macrophage reduction strategies such as selective killing of plaque macrophages by photodynamic therapy (PDT) and photothermal therapy (PTT) using photosensitizers such as dextran coated gold nanorods or single walled carbon nanotubes[6]. Although somewhat effective, such therapies have limited light penetration and can cause significant collateral tissue damage. In contrast, macrophage selective interventions that deliver small-molecule therapeutics, oligonucleotides or biologics can avoid potential tissue damage, diminish unwanted side effects, and provide opportunity to manipulate the cells' immune response[7].

Our laboratory, among others, has been working on the detection of inflammatory cell populations in experimental disease models such as atherosclerosis and type 2 diabetes[8–10]. We set out to develop a “universal” nanoparticle probe capable of incorporating a variety of imaging probes and therapeutic drugs with targeted delivery to M1 macrophages. Towards this goal, we turned our attention to commercially available polystyrene latex as model nanoparticles and fine research tool. Polystyrene nanoparticles have been used as model nanoparticles to study mechanism of nanoparticle drug delivery carrier uptake and processing in macrophages[11–14]. Latex nanoparticles are inexpensive, stable at high salt and protein content, and can be easily modified via passive adsorption or covalently bound to biomolecules[15,16]. Importantly, bare latex nanoparticles have been shown to selectively label inflammatory monocytes and macrophages in pathologies such as atherosclerosis, diabetes, and airway infection though the efficiency was relatively low[17,18].

In this study, we report lipid–latex (LiLa) hybrid nanoparticles targeting inflammatory macrophages. As shown in Fig. 1, the latex core served as a model hydrophobic polymeric template and the lipids provided targeting functionality and colloidal stability. Targeting to inflammatory macrophages was achieved by coating LiLa with phosphatidylserine (PtdSer) and oxidized cholesterol ester derivative cholesterol-9-carboxynonanoate (9-CCN). These lipids, sometimes called “eat-me” signals, are efficiently phagocytized by macrophages[8,19]. We previously used PtdSer and 9-CCN in different nanoparticles to target and image macrophages in atherosclerosis, however, to our knowledge there are no prior reports of a theranostic nanocarrier using “eat-me” signals that can accommodate hydrophobic dye/drug molecules in any combination and size (latex nanoparticles and spheres are commercially available in sizes from 20 nm to 10  $\mu$ m). This makes LiLa particles truly versatile and suitable for high-throughput nanoparticle screening. The selectivity of LiLa to image pro-inflammatory macrophages was tested in two disease models: (i) an experimental atherosclerosis model, where macrophages were imaged non-invasively through magnetic resonance imaging (MRI)[4, 7]; and (ii) a model of diet induced obesity, where pro-inflammatory macrophages were identified using intravital fluorescence imaging of adipose pad. In addition, we tested whether LiLa nanoparticles can serve as efficient theranostics for inflammation. These prototypical LiLa nanoparticles are schematically depicted in Fig. 1.

## 2. Results

### 2.1. Synthesis and characterization of LiLa nanoparticles

LiLa nanoparticles were synthesized through a one-step self-assembly after hydration of lipid film with 4% aqueous polystyrene latex nanoparticles (40 nm in diameter) followed by fast bath sonication. All lipid films contained 2–5 mol% of PtdSer and 9-CCN, 5 mol% of phosphatidylethanolamine-PEG2000 and varying concentrations of contrast agents, drug and dyes (see below and Supporting Information). We discovered that the lipid film may include up to 7 mol% of hydrophobic entities in any combination, thus allowing for controlled synthesis of particles with desired functionality (Fig. 1). With the aim of creating theranostic MRI-visible nanoparticles, that can be tracked via fluorescence and effectively shorten

longitudinal (T1) relaxation time, we prepared nanoparticles bearing gadolinium DTPA-bis(stearylamide) [Gd-DTPA-SA] using fluorescent (FITC) latex core.

The assembly of lipid layer on latex nanoparticles was tested across a number of formulations obtained by hydrating 0.2–16 mg of lipid film with 4% of latex nanoparticles for optimal size and stability of LiLa nanoparticles. As shown in Fig. 2a, dynamic light scattering measurements indicated the formation of larger, heterogeneous particles with lipid content >1.5 mg, possibly due to the formation of mixed micelles and large vesicles encapsulating multiple latex cores. A molar ratio of 1.5 mg of lipids per 1 mg of latex provided the best compromise between size ( $65 \pm 10$  nm) and polydispersity (PDI) [ $0.11 \pm 0.05$ ] for Gd-FITC-LiLa particle formulation (lead formulation). Cryo-transmission electron microscopy (cryo-TEM) confirmed that Gd-LiLa particles consisted of a latex core decorated with a lipid-PEG layer, as seen by the outer corona (white arrowheads on Fig. 2b). The electron-dense dark spots (yellow arrows on Fig. 2b) seen on the surface of the latex core most likely indicate the Gd-lipids. The magnetic properties of Gd-FITC-LiLa longitudinal (T1) relaxation times of protons in water solutions of Gd-LiLa were measured at a clinically-relevant magnetic field strength of 1.5 T (Fig. 2c). The r1 relaxivity for Gd-FITC-LiLa ( $8.3 \text{ mM}^{-1} \text{ s}^{-1}$ ) was 2-fold higher than clinically approved Magnevist Gd-DTPA ( $4.0 \text{ mM}^{-1} \text{ s}^{-1}$ )[20]. The Gd-LiLa formulation was highly stable in PBS buffer and 10% human plasma even at 48 h as compared to bare-latex nanoparticles that appeared turbid immediately after mixing with 10% human plasma (Fig. S2). Size measurements of Gd-LiLa and bare latex in human plasma or PBS have confirmed superior stability of Gd-LiLa (Table 1).

## 2.2. Drug loading and release

To determine whether LiLa can incorporate small molecule therapeutics along with Gd-DTPA-SA and lipids, we studied Gd-LiLa drug loading capacity with three model hydrophobic drugs: Rosiglitazone (Rosi), Paclitaxel (PAX) and tamoxifen (TAM). All the drugs displayed high binding to LiLa (Fig. 2d and Table S4), with Rosi being the most efficient ( $0.59 \pm 0.15$  mg of drug per 1 mg of latex), whereas PAX and TAM incorporation was  $0.14 \pm 0.07$  mg and  $0.48 \pm 0.39$  mg of drug per 1 mg of latex respectively (Table S4 in Supplementary Information). Next, we investigated drug release via dynamic dialysis release experiments using Rosi-LiLa as a model formulation. The release of Rosi from Rosi-LiLa particles incubated in 50% human plasma for 72 h at 37 °C was less than 4% (as measured by LC-MS; Fig. 2e).

## 2.3. LiLa nanoparticles selectively target inflammatory M1-macrophages in vitro

We aimed to test Gd-FITC-LiLa in human and mouse atherosclerosis-relevant in vitro systems: 1) murine fibroblast cell line (L-cells), 2) human umbilical vein endothelial cells (HUVECs), and 3) murine RAW 264.7 macrophages. The Gd-FITC-LiLa was efficiently internalized by macrophages after 4 h of incubation at 37 °C. Fig. 3a illustrates that the RAW 264.7 macrophages showed high uptake of Gd-LiLa particles (i.e., 100% of the cells were particle-positive after 4 h) while L-cells and HUVEC cells were only somewhat efficient in nanoparticle uptake. The Gd-FITC-LiLa were observed to localize in the lysosomal compartments of RAW 264.7 cells, but not in lysosomes of L-cells or HUVECs

(Fig. 3a). Co-localization was evident after merging micrographs of Gd-FITC-LiLa fluorescence with that of immunofluorescence of lysosomal-associated membrane protein 1 (LAMP1). Next, the kinetics of Gd-FITC-LiLa cellular uptake in these cells was measured by quantifying cell fluorescence at various time points using a plate reader (Fig. 3b). RAW 264.7 cells demonstrated rapid, linear uptake over 24 h incubation. Conversely, the uptake in L-Cells and HUVECs was blunted and reached saturation at 8 h.

Next, differential uptake of LiLa bearing AlexaFluor 647 was studied in two major sub-types of macrophages (M1, M2) using imaging flow cytometry. M1- and M2-macrophages were prepared using bone-marrow derived macrophages from wild-type C57BL/6 mice as previously described[21]. The polarization of the resting macrophages into the M1 and M2 subtypes following stimulation was confirmed by measuring the mRNA expression of different markers characteristic for these phenotypes (Supporting Information, Fig. S4). The results of flow-cytometric analysis demonstrated that LiLa nanoparticles were taken up by M1-macrophages more efficiently than by M2-macrophages as seen in the histograms in Fig. 3c and d. The histogram representing LiLa uptake in M1 macrophages (Fig. 3d, filled red) is shifted, indicating increased fluorescence levels in these cells as compared with M2 cells. Conversely, bare latex nanoparticles did not demonstrate the selectivity in uptake (Fig. 3c). To visualize the uptake on a single cell level, Amnis FlowSight imaging was used to microscopically evaluate the localization of engulfed particles (Fig. 3c, d insets). The results demonstrate that the cells incubated with bare latex produce a somewhat diffuse staining, likely due to membrane-associated particles that were not yet internalized. Similar appearance of the LiLa staining was noted in M2 macrophages (Fig. 3d, bottom inset). In contrast, highly localized, punctate staining of LiLa nanoparticles was observed in M1-macrophages (Fig. 3d, middle inset). The latter could indicate nanoparticle internalization and the accumulation in intracellular compartments, likely in lysosomes, as demonstrated above in RAW 264.7 macrophages (Fig. 3a). Taken together, these results indicate that the M1 macrophages preferentially engulf LiLa nanoparticles, likely through the phagocytic signals that also mediate rapid intracellular localization[22].

#### 2.4. Anti-inflammatory LiLa nanoparticles dampen macrophage inflammation

We next studied whether drug-loaded LiLa is therapeutically active *in vitro* by investigating the anti-inflammatory effects of Rosi-LiLa in pro-inflammatory macrophages. The RAW 264.7 macrophages were polarized to M1 inflammatory phenotype by stimulation with 100 ng/mL lipopolysaccharide (LPS) for 24 h. The M1 phenotype was confirmed using flow cytometry by surface marker Ly6C immunostaining (Fig. 4a, b). The results show that LPS-stimulated cells demonstrated significantly higher surface expression of Ly6C as compared to unstimulated cells. The significant increase in levels of the proinflammatory cytokines (sometimes called Th1 response) such as TNF- $\alpha$ , IL-6 and CCL-2 in cell culture media of LPS-treated macrophages was also an indicator of “M1”-phenotype (Fig. 4a,b) and (Supporting Information, Fig. S5)[23]. Third, we ensured that concentrations of free and nanoparticle-bound drug added to the cells were identical (100 ng/mL) by measuring Rosi concentrations by LC-MS (supporting information-methods) just before the experiment. After an exposure of cells to bare latex, free Rosi, and Rosi-LiLa for 4 h, we analyzed a panel of inflammation-associated cytokines using BD Biosciences Cytometric Bead Array.

We observed a significant decrease in the concentration of the Th1 cytokines (TNF- $\alpha$ , CCL-2, and IL-6) in cells treated with Rosi-LiLa and Rosi but not bare latex. Rosi-LiLa was as efficient as Rosi alone in dampening inflammation (Fig. 4c). Similar trend was observed at the transcriptional level with quantitative RT-PCR (Fig. 4d).

## 2.5. Controlled release of the cargo from LiLa nanoparticles is phospholipase A2-dependent

LiLa particles are highly stable, possibly due to protective lipid shell (Fig. 1). At the same time, the phospholipase A2 (PLA2) is known to rapidly degrade phospholipids, particularly when the phospholipid shell is presented on nanoparticle surface[24]. We speculated that latex particles that are devoid of lipid shell will have significantly reduced stability in physiological environment. To investigate the possibility of PLA2-triggered LiLa degradation, we first designed and synthesized LiLa nanoparticles equipped with Förster resonance energy transfer (FRET) properties that could be regulated by PLA2. FRET-LiLa beacon (Fig. 5a) was synthesized from fluorescein-cored latex (FRET donor) and a model drug rhodamine (FRET acceptor), the latex core and phospholipid layer. Non-FRET controls were also synthesized and included: FITC-LiLa, where fluorescein is incorporated in the core without lipids, and Rhod-LiLa, where rhodamine dye is absorbed on the bare latex nanoparticles (without FITC) and covered with lipids as usual.

To confirm FRET, the fluorescence spectra of FRET-LiLa in deionized water or methanol was recorded on a spectrofluorometer with a 460-nm excitation. The FRET-LiLa exhibited a strong 550 nm emission signal due to the energy transfer from fluorescein to rhodamine when present in close proximity to each other. Methanol decomposition of FRET-LiLa resulted in FRET loss as detected by a concurrent increase in fluorescein emission at 480 nm and disappearance of the 550 nm peak (Fig. 5b). We then incubated snake-venom PLA2 (*Naja mossambica*) with FRET-LiLa or single-fluorophore LiLa particles serving as non-FRET controls. Fig. 5c demonstrates time course fluorescence response of FRET and non-FRET beacons monitored at a 480 nm emission using plate reader. The results show that the PLA2 produced a rapid and saturated FRET loss response in FRET-LiLa as compared to non-FRET LiLa controls, indicating the occurrence of enzymatically-triggered rhodamine release. Slight increase in 480 nm emission from non-FRET rhodamine-LiLa (Rhod-LiLa) was due to, perhaps, the increase in fluorescence intensity of the bulk-released rhodamine, which was otherwise locally self-quenched in LiLa nanoparticles. The intracellular PLA2-mediated drug release from FRET-LiLa was assessed in macrophages. RAW 264.7 macrophages were pretreated for 24 h with or without 20  $\mu$ M methyl arachidonyl fluorophosphonate (MAFP, an inhibitor of PLA2)[25] and then incubated with FRET-LiLa nanoparticles for 4 h, followed by confocal microscopy analysis. To quantify the FRET loss we employed sensitized emission FRET confocal microscopy for analysis of FRET efficiency and distance (see Supporting Information for method details)[26]. Fig. 5d and e illustrates an outcome of these measurements presented as processed FRET (pFRET) micrographs indicating FRET-positive areas inside of the cells. Cells that were treated with MAFP, PLA2 inhibitor, were observed to have greater FRET efficiency (0.77 vs 0.48) and smaller distance (8.3 nm vs 9.2 nm) as compared to untreated cells suggesting the detachment of rhodamine from LiLa particles in a PLA2-dependent manner.

We next investigated the role of phospholipids in the “protection” of latex-adsorbed molecules when LiLa was exposed to human serum. The nanoparticles containing Rhodamine with and without phospholipids (Rhod-Latex and Rhod-LiLa respectively) were incubated in PBS or 30% human serum at 37 °C, and the fluorescence emission spectra of rhodamine were recorded over time. It is well known that rhodamine fluorescence is highly sensitive to self-quenching[27–29]. The spectra in PBS indicate that the emission intensity of rhodamine is similar in both formulations and is likely self-quenched due to high local concentration of the rhodamine on the surface of the nanoparticles. However, when the nanoparticles were subjected to human serum, Rhod-Latex exhibited a 4.5-fold increase in the fluorescence intensity as compared to Rhod-LiLa (Fig. 5f). Next, we investigated whether “protective” effect can be reduced when phospholipids are partially degraded by PLA2. Because it is very difficult to control the enzymatic reaction to obtain LiLa with partially-degraded phospholipids, we synthesized Rhod-LysoPC-Latex, where 50% of phosphatidylcholine (PC) in LiLa, was replaced with Lyso-PC, a product of PLA2 enzymatic activity on PC (Fig. 5a inset). We incubated Rhod-LysoPC-Latex with human serum same as in above experiments and recorded fluorescence emission over time. In contrast to burst release from Rhod-Latex, Rhod-LysoPC-Latex demonstrated gradual, sustained release of the rhodamine as indicated by steadily increasing emission intensity over time (Fig. 5f). These results along with FRET data described above indicate that the protective phospholipid shell is needed for latex-adsorbed molecules to be carried in physiological environment.

## 2.6. Molecular MRI with Gd-FITC-LiLa detects inflammatory macrophages

To test in vivo imaging characteristics of Gd-FITC-LiLa and the ability to image inflammatory macrophages, we have performed magnetic resonance (MR) imaging with Gd-LiLa serving as a contrast agent. The testing was performed in apolipoprotein E knockout mice (ApoE<sup>-/-</sup>, KO), a well-known model of inflammation and atherosclerosis. Dynamic MR imaging of Gd-FITC-LiLa nanoparticles enabled sustained visualization of the vasculature as shown in maximum intensity projection T1-weighted scans (Fig. 6a). MR images show that contrast-enhanced blood-pool signal was stable up to 2 h after Gd-FITC-LiLa injection in WT mice and allowed for identification of descending abdominal aorta (A), celiac trunk (C), superior mesenteric artery (M), and at least one kidney (K). Importantly, the contrast kinetics suggested significantly prolonged persistence of Gd-FITC-LiLa in the circulation of WT mice with a half-life of  $t_{1/2} = 49$  min, as compared to that in KO mice with  $t_{1/2} = 12$  min. Fast blood clearance of Gd-FITC-LiLa in KO mice prompted us to speculate that this is the result of the preferential and rapid uptake of Gd-LiLa by inflammatory monocytes in circulation and “M1”-like macrophages in major organs. Pharmacokinetic experiments (Fig. 6b) performed on a separate set (n = 7) of WT and KO mice injected with Gd-FITC-LiLa confirmed the longer residence time in circulation ( $t_{1/2} = 63$  min) of Gd-FITC-LiLa in WT mice as compared to that in KO animals ( $t_{1/2} = 13$  min).

Further, we also investigated plaque associated macrophage uptake of Gd-FITC-LiLa nanoparticles by MR imaging of the abdominal aorta using T1-weighted gradient-echo sequence developed in our laboratory[8–10]. Gd-FITC-LiLa nanoparticles were injected into KO and WT animals (n = 3–4 per group) followed by MR imaging of the abdominal aorta.

Fig. 6c shows axial multiplanar images that demonstrate prominent Gd-FITC-LiLa accumulation in the vascular wall (arrows) of KO but not WT animals. Quantitative analysis of contrast enhancement expressed as a ratio of signal intensity in plaque vs that in muscle confirmed visual observation of MR scans (Supporting Information Fig. S6).

Cell-specific deposition of Gd-FITC-LiLa in plaque was further evaluated by examining aortic tissue sections by confocal microscopy. Fig. 6d and e shows representative fluorescence micrographs of aortic tissue from KO mice injected with Gd-FITC-LiLa. Staining with macrophage specific marker F4/80 and nuclear dye DAPI allowed for visualization of nanoparticles within the macrophages. The merged fluorescence signal from Gd-FITC-LiLa (green), macrophage specific marker F4/80 (red) (blue) appeared yellow, indicating strong co-localization between Gd-FITC-LiLa and macrophages. Conversely, a much smaller number of Gd-FITC-LiLa nanoparticles in aorta of WT animals were detected. Consistent with this finding, there was no observable co-staining of Gd-FITC-LiLa (green) and macrophage specific marker F4/80 (red) in aortic tissue sections of WT mice (Supporting information Fig. S7). Interestingly, Gd-FITC-LiLa appeared to deposit to the shoulder of the atherosclerotic lesions in KO mice (Fig. 6d, asterisk).

The biodistribution of Gd-FITC-LiLa nanoparticles indicated a substantial difference in nanoparticle levels between KO and WT mice (Supporting information Fig. S8). The intravenously injected Gd-FITC-LiLa were predominantly taken up by the spleen, liver, aorta and to a lesser extent in lungs and heart, followed by kidneys and adipose, as reported for nanoparticles 100 nm [30]. Consistent with our imaging data, the Gd-FITC-LiLa was found at high concentrations in the atherosclerotic plaque of KO mice compared to bare latex nanoparticles that accumulated to a large extent in the liver (supporting information Fig. S9). In addition, cell-specific distribution in these tissues was investigated by immunohistochemistry of tissue sections with F4/80 antibody (detecting macrophages) and anti-CD31 antibodies (detecting endothelial cells). The results show that Gd-FITC-LiLa strongly co-localized with macrophages (Supporting Information, Fig. S7), but minimally in CD31-positive endothelial cells in liver, spleen, aorta, heart, kidney tissues. Taken together, these results suggest that LiLa nanoparticles preferentially target inflammatory “M1” macrophages allowing for effective imaging of vasculature and atherosclerosis.

## **2.7. LiLa nanoparticles enable intravital near-infrared fluorescence imaging and selectively accumulate in inflammatory macrophages within the adipose tissue**

Having demonstrated the utility of Gd-LiLa nanoparticles for selective MR imaging of pro-inflammatory “M1” macrophages in atherosclerosis, we then turned to explore the scope of molecular imaging of these cells in the adipose tissue. Molecular imaging of macrophages in adipose tissue was performed in a model of diet-induced obesity known to exhibit visceral adipose inflammation. In order to distinguish macrophages from other cell types *in vivo*, we took advantage of reporter mice where macrophages ubiquitously express the yellow fluorescent protein (YFP). Adipose tissue imaging was conducted with a time-lapse single-photon confocal intravital microscope, built in-house on the basis of the VisiTech Infinity3 system (see Fig. 7a and Supporting Information for details) and using AlexaFluor 647 nanoparticles (AF647-LiLa) as a contrast agent. We used obese *c-fms*<sup>YFP+</sup> mice as a



convenient model of M1-macrophage enriched adipose[31], which was termed “M1-model” because their adipose tissue best resembles clinical obesity. Control animals (lean) were termed an “M2-model”, given the fact that the healthy adipose tissue is populated by macrophages with distinct “M2” features[23].

Confocal time-lapse imaging of adipose enabled robust identification of macrophages that were detected by their intrinsic YFP fluorescence at an excitation of 514 nm and emission maxima at 527 nm (Fig. 7b and c). We then injected AF647-LiLa into our M1- and M2-models and monitored the uptake over time. The AF647-LiLa injection produced bright and stable red fluorescence signal observed in the adipose blood vessels (Supporting Information Movie 1). Fig. 7b and c shows images of the adipose at different time points indicating the uptake of AF647-LiLa (red) by YFP<sup>+</sup>-macrophages (green). AF647-LiLa were observed to localize at junctions of adipocytes (characteristic hexagonal-like shaped large cells) and co-localize with YFP<sup>+</sup> macrophages (arrows, Fig. 7b, c). We observed that macrophages concentrated particles ~20 min after injection in M1-model, whereas, in M2-model, the deposition of LiLa was mostly noted in junctions of adipocytes, and to the lesser extent in YFP<sup>+</sup> cells. The rapid accumulation of LiLa in inflammatory macrophages of M1-model was also observed through quantitative image analysis. The average of the AF647-LiLa fluorescence intensity in YFP<sup>+</sup> cells for each frame was recorded and a time vs nanoparticle fluorescence intensity plot was generated (Fig. 7d). By comparing the area under the curve (AUC) from M1-model vs M2-model, we determined the relative uptake of AF647-LiLa by macrophages (“M1” vs “M2”) in the adipose tissue (Fig. 7e). We also observed that the initial peak fluorescence in M1-model was significantly higher than that in the M2-model.

### 3. Discussion

We found that latex nanoparticles can be easily decorated with macrophage targeting phospholipid components phosphatidylserine (PtdSer) and oxidized cholesterol ester derivative cholesterol-9-carboxynanoate (9-CCN) resulting in lipid–latex hybrid nanoparticles (LiLa), where the latex core served as a model size-determining template and lipid/hydrophobic entities provided functionality. These lipids, sometimes called “eat-me” signals, are efficiently phagocytized by macrophages[9,19]. We previously used PtdSer and 9-CCN in different nanoparticles to target and image macrophages in atherosclerosis, however, to our knowledge there are no prior reports of a theranostic nanocarrier using “eat-me” signals that can accommodate hydrophobic dye/drug molecules in any combination and size (latex nanoparticles and spheres are commercially available in sizes from 20 nm to 10  $\mu$ m). This makes LiLa particles truly versatile and a model research tool.

The hydrodynamic diameter of Gd-LiLa was  $65 \pm 10$  nm and particles were colloiddally stable in PBS buffer and 10% human plasma at 37 °C as compared to bare latex nanoparticles (Table 1 and Figs. S1–S2). It is well documented that nanoparticle size determines in vivo pharmacokinetics with nanoparticles spanning a range of sizes from 50 to 100 nm being the most favorable for tissue penetration after systemic administration[32]. Therefore; we selected this Gd-FITC-LiLa as “lead” formulation for all future studies. We observed two fold higher  $r_1$  relaxivity for Gd-FITC-LiLa as compared to a commercial agent Magnevist, which is likely due to the result of reduced tumbling rate resulting from

anchoring of Gd chelates to the external surface of the latex and the consequent increase in rotational correlation time of the bound contrast agent[33]. The dynamic dialysis experiments of Rosi-LiLa in 50% human plasma showed less than 4% release at 72 h at 37 °C (Fig. 2e). These results indicate that theranostic LiLa nanoparticles can stably carry drug payloads in physiological environment and thus act as highly efficient, controlled drug delivery carriers.

The drug loading efficiency of Rosi was the highest as compared to tamoxifen (TAM) and paclitaxel (PAX) due to positive charge of the Rosi molecule carrying an aminopyridine fragment (Fig. 2, Table S4). We speculate that slightly positive charge of Rosi allows higher loading due to electrostatic interaction with the negatively charged latex nanoparticles. Similar effect is often observed for positively charged doxorubicin, known to exhibit superior loading when encapsulated within negatively charged nanomaterials[34]. Paclitaxel is known to have decreased stability in aqueous solutions and mixture of aqueous and organic solvents. The relatively low stability of paclitaxel may have contributed to its minimal loading on LiLa particles[35].

We believe that all molecules and probes used in LiLa are “sandwiched” between the latex core and the phospholipid shell. The latter serves as an outer “protective” layer along with PEG (that is also a part of phospholipid assembly as phosphoethanolamine-PEG). Our assumptions are based on two lines of evidence and existing literature on polymer–lipid hybrid nanoparticles. First, our cryo-TEM investigation led us to believe that phospholipids are presented via monolayer on the surface sub-100 nm latex, similar to PLGA- or silica-based hybrids that are frequently used for drug delivery by research groups of R. Langer, O. Farokhzad and others[36–38], and have been shown to have distinct phospholipid monolayer[36–38]. Given the similarity of LiLa to these nanosystems in terms of size and composition, and our DLS and cryo-TEM investigations, we are confident that LiLa is covered by a monolayer of phospholipids.

Second, when the nanoparticles containing rhodamine with and without phospholipids were incubated in 30% human plasma, the presence of phospholipid shell in Rhod-LiLa prevented dye leakage even after 2 h of incubation. The stability of the system was drastically decreased when PC phospholipids were replaced with lyso-PC. Lysophospholipids are known to serve as detergents disrupting phospholipid membranes, change organization of phospholipids in the membrane, and tilt hydrophobic chains allowing for facilitated exchange between inner membrane and outer membrane molecules.

Having demonstrated preferential uptake of LiLa nanoparticles by macrophages (Fig. 3a, b), we next tested the possibility of differential uptake of LiLa between two major sub-types of macrophages. The role of a macrophage in a tissue is largely governed by the polarization state, which determines the pro- or anti-inflammatory and phagocytic potential. Macrophage polarization is likely a continuous scale, while the extremes in polarization are well characteristic[23]. Thus, bone marrow- or peritoneal-derived macrophages stimulated with LPS are referred to as M1-phenotype and characterized by a high expression level of pro-inflammatory molecules such as iNOS, TNF- $\alpha$ , and IL-6. In contrast, M2 macrophages are prepared via stimulation with IL-4 and express high levels of CD206 and Arginase-1

(Arg-1). While the process of macrophage phenotyping is an ongoing debate, it is well recognized that M1-like macrophages potentiate inflammatory processes in diseases of such as atherosclerosis and obesity. Therefore, we next investigated whether the uptake of LiLa nanoparticles differs in M1- and M2-polarized macrophages. The results from imaging flow cytometry studies show that LiLa particles are engulfed to a higher extent in M1 macrophages, and demonstrate a distinct punctate accumulation pattern indicating lysosomal localization within M1 macrophages (Fig. 3c, d).

LiLa nanoparticles can serve as efficient vehicles for intracellular delivery of therapeutics as indicated by our experiments in RAW 264.7 macrophages after treatment with bare-latex, free drug Rosi and Rosi-LiLa nanoparticles (Fig. 4). We chose Rosiglitazone (Rosi) as a model drug, as it is a high-potency peroxisome proliferator-activated receptor (PPAR)  $\gamma$  agonist with anti-inflammatory effects [39]. Although, Rosi suffers from severe side effects, including weight gain and congestive heart failure and was recently withdrawn from clinical use[40]. It is, however, a powerful model drug routinely used in diabetes and obesity research, that is able to modulate inflammatory and immune responses in macrophages and trigger fast changes in gene expression[41–43]. The results showed a significant decrease in the concentration of the Th1 cytokines (TNF- $\alpha$ , CCL-2, and IL-6) in cells treated with Rosi-LiLa and free Rosi. However, we reason that free Rosi and Rosi-LiLa, although taken up by in macrophages through a different pathways (passive diffusion for free drug versus receptor-mediated uptake for Rosi-LiLa), provide similar functional effect due to 1) identical amount of Rosi used in both cases, as confirmed by LC–MS just before the incubation with cells; and 2) possible saturation of the binding site of the nuclear receptor at the concentration of Rosi used in this study. This resulted in almost identical changes in downregulation of inflammatory gene expression.

It is somewhat surprising that Rosi-LiLa nanoparticles eluting <4% of their payload over 72 h (Fig. 2e) show a pronounced anti-inflammatory effects in macrophages after 4 h of incubation (Fig. 4). Therefore, we asked the question: how do LiLa nanoparticles release their cargo when engulfed by the cell? It has been suggested that nanoparticles with the polymeric core incorporating hydrophobic drugs and “decorated” with phospholipid exterior layer have increased stability and delayed drug release[44]. On the other hand, the rate of the degradation of phospholipids by phospholipases increases significantly when the phospholipid layer is presented on the surface of nanoparticles[24]. We, therefore, investigated whether the drug release mechanism from LiLa nanoparticles is facilitated by intracellular phospholipases. Phospholipase A2 (PLA2) is known to be significantly upregulated in in-flammatory macrophages and found at high concentrations in atherosclerosis[45–48]. The results show that the PLA2 produced a rapid and saturated FRET loss response in FRET-LiLa as compared to non-FRET LiLa controls, indicating the occurrence of enzymatically-triggered rhodamine release (Fig. 5c). The intracellular FRET efficiency measurements in macrophages after addition of PLA2 inhibitor indicate greater FRET efficiency and smaller distance as compared to untreated cells. These results show that enhanced activity of PLA2 towards phospholipid layer on the LiLa surface may result in facilitated drug release, which manifests in therapeutic actions of Rosi-LiLa demonstrated in Fig. 4.

It is well established that “M1”-like macrophages are present in progressing atherosclerotic plaques[23] and that their numbers may increase drastically as a result of plaque-infiltrating inflammatory Ly6C<sup>high</sup> monocytes, especially in response to hyperglycemia[49], myocardial infarction[50], and stress[51]. These cells are characterized by high phagocytic capacity demonstrating progressive uptake of lipids and oxidized lipoproteins, which becomes more pronounced in progressing atherosclerosis[23,52]. Conversely, “M2”-macrophages are highly-efficient during their homeostatic role in clearing apoptotic cells (in the process called efferocytosis), but become phagocytically impaired in progressing atherosclerotic plaques[53]. Here, we reasoned that “M1”-macrophages and Ly6C<sup>high</sup> monocytes, being intrinsically more efficient phagocytes when compared to other cells in advanced atherosclerosis, can be selectively discerned by hyper-uptake of Gd-LiLa in MRI, allowing for “molecular imaging”. To test this hypothesis in vivo, we have chosen a well-validated animal model of atherosclerosis, apolipoprotein E knockout mice (ApoE<sup>-/-</sup>, KO). The deletion of ApoE gene transcripts in mice not only provides a useful preclinical model of atherosclerosis with features similar to human disease[54], but also gives rise to macrophages that are ubiquitously skewed to an “M1”-phenotype[55,56].

Macrophage targeted molecular dynamic MR imaging and pharmacokinetic experiments showed that Gd-LiLa particles decreased half-life in KO mice as compared with WT controls. The fast clearance from circulation could likely be attributed to uptake by the inflammatory monocytes in circulation and “M1”-like macrophages in major organs. It is well known that nanoparticles with a diameter of sub-100 nm penetrate “leaky” vasculature and become accessible for macrophages in sub-endothelial space[32]. We further investigated whether Gd-LiLa can deposit in plaque-associated macrophages allowing non-invasive imaging of abdominal aorta. MRI scans demonstrated prominent Gd-LiLa accumulation in the vascular wall (Fig. 6c). This result was also confirmed by ex vivo immunohistochemistry of aortic sections by confocal microscopy, that showed colocalization of Gd-LiLa and macrophage marker F4/80. We found that Gd-LiLa appeared to deposit to the shoulder of the atherosclerotic lesions in KO mice (Fig. 6d, asterisk). It is well known that the shoulder region of plaque is extensively infiltrated by macrophages and characterized by increased inflammation and shear stress, also being the site where plaque rupture is most commonly observed[57].

The biodistribution of Gd-LiLa nanoparticles studied by LC-MS showed that Gd and Rosi were detected at high concentration in the plaque, demonstrating the drug delivery capability of LiLa (Supporting information Fig. S8). Immunohistochemistry of tissue sections also confirmed the preferential targeting of LiLa nanoparticles to macrophages in the liver, spleen, aorta and minimal presence in lungs, kidneys in KO mice (Supporting information Fig. S7). The biodistribution study demonstrated that two key tissues of interest (atherosclerotic aorta and fatty adipose) can be selectively targeted by LiLa particles because of the presence of M1 macrophages. We also observed some accumulation in lungs (Fig. S8). Interestingly, the lung tissue of KO mice were targeted by LiLa-NPs, as compared to minimal targeting in WT mice. We also posited that lipid and PEG layer on LiLa may decrease lung deposition as compared to bare latex or other NPs such as silica NPs. Thus, in a study by Z. Fayad and colleagues it was shown that silica NPs significantly deposited to lungs due to aggregation, whereas PEGylated silica-lipid hybrid NPs showed minimal lung

uptake[58]. The specificity of LiLa to “M1”-macrophages in plaque and other tissues may still have to be confirmed, however, this is beyond the scope of this proof-of-principle study. We also envision that the rapid-clearance of Gd-LiLa may provide superior intravascular MR enhancement and reduced toxicity[59].

Although adipocytes are the major cell type that constitutes healthy adipose tissue, macrophages are found at increased numbers in the visceral fat depots of obese humans and mice[60]. Macrophage polarization plays a critical role in initiation and progression of obesity and comorbidities such as metabolic disease (insulin resistance). Metabolic abnormalities caused by obesity have been shown to polarize adipose tissue macrophages from an “M2” to an “M1” phenotype inducing inflammation via Th1-type pro-inflammatory cytokines[23,61]. Molecular imaging of “M1”-cells in obesity may allow non-invasive assessment of adipose tissue inflammation and identify individuals at risk for insulin resistance. To perform adipose tissue imaging, we have previously demonstrated that c-fms YFP<sup>+</sup> mice on an FVBN background are characterized by stable and selective expression of YFP in Ly6C<sup>high</sup> F4/80<sup>+</sup> leukocytes, the precursors of pro-inflammatory “M1”-macrophages in the adipose[31,62]. Due to intrinsic bright YFP fluorescence these cells can be conveniently detected using intravital microscopy in living animals. Adipose tissue imaging confirmed the accumulation of AlexaFluor 647 nanoparticles (AF647-LiLa) at junctions of adipocytes (characteristic hexagonal-like shaped large cells) and co-localized with YFP<sup>+</sup> macrophages and a higher accumulation was observed in M1 model compared to M2 model showing the uptake of AF647-LiLa as a function of macrophage phenotype (Fig. 7).

Taken together, these data support use of LiLa nanoparticles as a model research tool for intravital imaging. Early time-point imaging data (<10 min after injection) indicate that LiLa nanoparticles allow for clear visualization of the adipose vascular system, a property that might be useful for imaging of other highly vascular sites such as neovascularized tumors[63]. Most importantly, our data show that the model LiLa nanoparticles target subsets of macrophages effectively by exploiting differential phagocytic ability among macrophage phenotypes (M1, M2) with avid accumulation of “eat-me” signal-containing LiLa nanoparticles by inflammatory adipose macrophages. This opens the possibility of further developing LiLa-like nanoparticles with biocompatible polymers as novel agents for “molecular imaging” of obesity and obesity-related chronic diseases.

#### 4. Conclusions

The goals of this study were: 1) to develop a simple, yet versatile multifunctional theranostic platform using readily available latex core as a model polymer and a fine research tool to assemble latex-lipid nanohybrids that could be synthesized in any laboratory and that met the drug delivery needs of the research community who might lack nanoparticle expertise or access to sophisticated manufacturing facilities; and 2) to demonstrate that phagocytic “eat-me” signals can preferentially target inflammatory macrophages in experimental models of atherosclerosis and adipose tissue inflammation opening the possibility of future clinical applications that diagnose/treat these conditions. We acknowledge that due to poor biodegradability of polystyrene, LiLa nanoparticles are unlikely to pass regulatory

requirements for clinical translation. We believe, however, that principles of phagocytic targeting employed here can be generalized to any other biocompatible and biodegradable nanoparticles including those on “fast-track” for clinical translation[32,64]. Our results suggest that the LiLa platform is a promising theranostic nanosystem with potential use in a myriad of research and pre-clinical endeavors focusing on novel therapies, targeting ligands or imaging approaches, rather than developing new drug delivery platform(s). The phagocytic targeting may be impactful in diseases where macrophage inflammation has pathophysiological relevance including cardiovascular disease, obesity, diabetes, and cancer. A highly exciting prospect with immediate clinical implications lies in “molecular imaging” through radiotracer phagocytic signals, a possibility that warrants future exploration.

## 5. Methods

### 5.1. Synthesis of LiLa nanoparticles

9.43 mg (12.0  $\mu\text{mol}$ ) of L- $\alpha$ -phosphatidylcholine, 2.43 mg (3.0  $\mu\text{mol}$ ) of 1,2-dioleoyl-*sn*-glycero-3-phospho-L-serine, 4.64 mg (12.0  $\mu\text{mol}$ ) of 9-CCN and 3.31 mg (3.0  $\mu\text{mol}$ ) of Gd-DTPA-SA were mixed in chloroform and evaporated to dryness under nitrogen stream. The resulting lipid film was hydrated with 500  $\mu\text{L}$  of 2 wt.% carboxylate modified latex particles (either fluorescein- or dark red/AlexaFluor647-cored from Life Technologies) and subjected to water-bath ultrasonication using Misonix Sonicator 3000 for 10 min at room temperature to obtain gadolinium lipid–latex nanoparticles (Gd-FITC-LiLa).

### 5.2. Drug loading, encapsulation and loading efficiencies

To load the LiLa particles with hydrophobic drugs, the solutions of rosiglitazone (Rosi), tamoxifen (TAM), and paclitaxel (PAX), all at 1 mg/mL in methanol, were introduced to the lipid component, evaporated under nitrogen, and hydrated with latex nanoparticles as described above. Drug-LiLa nanoparticles were then purified by exhaustive dialysis against running tap deionized water using dialysis tubing with MW cutoff of 50 kDa (Sigma-Aldrich), and additionally by size-exclusion chromatography using 7 k MWCO Zeba centrifuge columns (Thermo-Pierce). To analyze the amount of drug remained in LiLa after purification, 100  $\mu\text{L}$  of nanoparticles were vigorously mixed with 240  $\mu\text{L}$  of methanol plus 10  $\mu\text{L}$  of 1  $\mu\text{g/mL}$  of internal standard in methanol (Tolbutamide analytical standard VETRANAL, Fluka), after which the precipitated polystyrene was separated by high-speed centrifugation (15 min  $\times$  25,000 *g*) and supernatant was collected in a separate tube. The polystyrene pellet was subjected to extraction with methanol in the same manner for three more times (total 4  $\times$  250  $\mu\text{L}$  methanol), following which combined extracts were evaporated under nitrogen gas, and the residue was reconstituted in HPLC mobile phase (acetonitrile:water 75:25). Analysis of drug concentration was next performed by LC–MS as described in Supporting Information. Drug concentrations were quantified with a standard curve. Peak areas were normalized to the spiked internal standard (Tolbutamide) to standardize between LC–MS runs and to account for deviation in extraction efficiency. The drug encapsulation (EE) and loading (LE) efficiencies were calculated using following equations: EE (%) = [total weight of drug in LiLa] / [weight of drug initially added]  $\times$  100%; LE (%) = [total weight of drug in LiLa] / [total weight of latex used]  $\times$  100%.

### 5.3. Drug release tests

The release of rosiglitazone (Rosi) from Gd-Rosi-LiLa was evaluated using a combination of dialysis and ultracentrifugal precipitation, which ensures separation of the proteins from nanoparticles. Thus, 100  $\mu\text{L}$  of Gd-Rosi-LiLa in PBS at 500  $\mu\text{g}$  Rosi per 1 mg polystyrene was mixed with 400  $\mu\text{L}$  of 50% human plasma and immediately distributed into dialysis chambers of eight Sigma Dispo-Biodialyzers (50  $\mu\text{L}$  each). Dispo-Biodialyzers were then immersed into a beaker containing 250 mL of preheated to 37  $^{\circ}\text{C}$  50% human plasma with stirring at 120 rpm. At the predetermined time point (1, 2, 4, 12, 24 and 72 h) one Dispo-Biodialyzer was removed and the sample was collected via centrifugation as per manufacturer's instructions. The sample was then diluted with 950  $\mu\text{L}$  of PBS and placed into an ultracentrifuge tube (Thermo). Next, the sample was ultracentrifuged in a Sorvall TFT-80.2 rotor at 50,000  $g$  for 1 h using Sorvall WX100 ultracentrifuge. The pelleted nanoparticles were then resuspended in 1 mL PBS via sonication, and ultracentrifugation was repeated. Each LiLa formulation at each time point was washed twice using ultracentrifugal precipitation as described above. The concentration of Rosi was measured in the pellet of LiLa after drug extraction with methanol in the presence of internal standard (see above) followed by LC-MS analysis (Supporting Information). The cumulative release percentage of Rosi from LiLa at each time point was calculated as: Rosi released (%) =  $(1 - [\text{total weight of Rosi in precipitate}] / [\text{total weight of Rosi in Gd-Rosi-LiLa}]) \times 100\%$ .

### 5.4. In vitro experiments

#### 5.4.1. Uptake of LiLa nanoparticles and visualization with confocal microscopy

—Cells were seeded on glass coverslips 24 h before use. After treatment with 2  $\mu\text{L}/\text{mL}$  of LiLa, the cells were washed three times with PBS, fixed with 4% formaldehyde for 10 min, and then permeabilized with 0.2% Triton X-100 for 5 min. Filamentous actin was labeled with AlexaFluor-546 phalloidin (Invitrogen) for 30 min according to manufacturer's instructions. For LAMP1 immunostaining, the cells were treated with various LiLa as mentioned above and in the text, fixed, permeabilized, blocked with 5% BSA in PBS for 1 h at room temperature, and incubated with rabbit anti-mouse LAMP1 primary antibody (Abcam) overnight at 4  $^{\circ}\text{C}$ . After washing extensively with PBS, the cells were incubated for 2 h at room temperature with donkey anti-rabbit AlexaFluor 647 secondary antibody (Life Technologies). All secondary antibody incubations were performed in the dark to minimize photo bleaching. The cells were then washed extensively in PBS, stained with DAPI (Life Technologies) for 10 min, and mounted on glass slides with Prolong Gold reagent (Life Technologies). The stained cells were imaged on an Olympus FV1000 spectral confocal microscope using 60 $\times$  objective.

**5.4.2. Therapeutic potential of LiLa nanoparticles**—RAW 264.7 cells were cultured in two 24-well plates according to conditions described above. One plate was treated with 100 ng/mL LPS and the second plate was left untreated. After 24 h of incubation, both plates were washed with sterile PBS three times and fresh media was added. Next, 1  $\mu\text{L}$  of concentration-adjusted Rosi-LiLa, Rosi alone, or bare latex (final concentration 100 ng/mL of Rosi, except bare latex) was added in both plates in quadruplicates. Four wells in each plate were left nanoparticle-free. Both plates were incubated for 4 h and then washed with PBS. Fresh media was added, and incubation was continued until the next day. After

incubation, the media was collected and stored at  $-80^{\circ}\text{C}$  until analysis via Inflammation 6-Plex Kit (see below). The cells were lysed using the lysis buffer supplied with Agilent RNA Miniprep Kit and the lysates were used for RNA isolation followed by quantitative real-time PCR analysis (Supporting Information).

**5.4.3. Inflammatory cytokine measurements**—Inflammatory cytokines were measured in cell media using mouse Inflammation 6-Plex Kit from BD Bioscience (San Diego, CA) according to manufacturer's instructions.

**5.4.4. PLA2-triggered drug release kinetic experiments**—One microliter of FRET-LiLa or control particles (FITC-LiLa, Rhod-LiLa) was mixed in a well of 96-well opaque microplate (6 wells per particle type) containing 99  $\mu\text{L}$  of 100 mM sodium acetate buffer (pH = 4.5), 0.5 mM calcium chloride and 0.1% bovine serum albumin. Plate was equilibrated at  $37^{\circ}\text{C}$  for 20 min in the cell culture incubator, sealed with PCR-grade adhesive film and placed into  $37^{\circ}\text{C}$ -preheated tray of Perkin Elmer Victor 3 fluorescence plate reader. Fluorescence measurements using 450 nm excitation filter and 480 nm emission filter were registered every 2 min for 6 min and then 20  $\mu\text{L}$  of enzyme solution in PBS containing 0.15 U/mL ( $\sim 2$  ng) PLA2 (Sigma-Aldrich P7778) was injected in each well and measurements were continued for thirty more minutes. Fluorescence intensity data was averaged for each particle type and data were presented as a % increase in 480 nm fluorescence.

## 5.5. Animals

All animal work was performed in AAALAC accredited facilities provided by The Ohio State University Laboratory Animal Resources (ULAR). The Institutional Animal Care and Use Committee (IACUC) approved the experimental animal protocols. Ten male ApoE<sup>-/-</sup> (KO) and six male C57BL/6 (WT) mice were obtained from Jackson Laboratories (Bar Harbor, ME). All KO animals were placed on a high-fat/high-cholesterol diet (0.2% total cholesterol, 42% calories from fat; Harlan Teklad, Madison, WI) ad libitum beginning at 15 weeks until 45 weeks of age. c-fmsYFP<sup>+</sup> transgenic mice were generated at the Transgenic Animal Service of Queensland, Brisbane, Queensland, Australia ([www.tasq.uq.edu.au](http://www.tasq.uq.edu.au)) by injection of the transgenes into pronuclei of (C57BL/6  $\times$  CBA)F1 (BCBF1) fertilized eggs as previously described [55]. YFP<sup>+</sup> were fed normal chow diet (M2-model, n = 3) or high fat diet for 15 weeks (M1-model, n = 3).

## 5.6. Magnetic resonance imaging

MRI was performed as previously described [10,11]. Briefly; MRI scans were performed using an 11.7 T Bruker MRI System (Billerica, MA, USA). Mice (n = 10 ApoE<sup>-/-</sup> and n = 6 WT) were anesthetized with inhaled isoflurane/O<sub>2</sub> gas mixture (maintenance: 1.5–2% of isoflurane) delivered through a nose cone and fixed head-up with paper tape in a 32 mm transmit/receive birdcage coil. A respiratory sensor was placed on the abdomen to monitor the depth and frequency of respiration to adjust the depth of anesthesia. A rectal probe monitored body temperature. After localization and acquisition of the pre contrast scan, each mouse was taken out of the magnet and injected with 100  $\mu\text{L}$  of Gd-LiLa (0.1 mmol/kg of Gd) via penile vein injection and immediately placed back in the magnet for the post



contrast scans. Each mouse was imaged for approximately 2 h after contrast administration using repetitive acquisitions of the 3D FLASH spin echo sequence. After the last 3D FLASH MRI scan, each mouse was taken out of the coil and kept in a quarantine facility for 24 h. After that, MRI scans were repeated using gradient echo sequence to image abdominal aortas as previously described [10,11].

### 5.7. Time-lapse confocal imaging of adipose pad

The diagram of the confocal microscope set-up used for real-time in vivo imaging of inflamed adipose is shown of Fig. 6a. The system was equipped with Olympus inverted microscope, Visitech Infinity 2D array confocal system (Sunderland, United Kingdom), and electron multiplying charge-coupled device (EMCCD, Hamamatsu, Hamamatsu Photonics, Japan). The basic optical path consisted of a stationary micro-lens array illuminated with an expanded laser beam. A galvanometer mirror scans the array over the sample and de-scans the returning fluorescence light. This light is separated from the illuminating beam by a dichroic mirror, and passes through a stationary pinhole array to create the confocal image. This image is re-scanned in perfect synchronization by the reverse side of the galvanometer mirror onto an EMCCD camera. The galvanometer scanner is readily synchronized to the selected camera exposure time and frame capture rate. All sequential images were obtained at 25 frames/s with the exposure time of 100 ms for each image. The Visitech system was equipped with an argon laser for excitation at 514 nm, and the emission signal was collected using a multidichroic mirror and 520 and 647 nm band-pass filters. Long Working Distance M Plan Semi-Apochromat (LMPLFLN) Olympus object lens ( $\times 20$  air) with numerical aperture 0.40 was used to visualize YFP<sup>+</sup> macrophages and AF647-LiLa<sup>+</sup> cells in adipose tissue.

### 5.8. Statistical analysis

Data are presented as the mean  $\pm$  SD. Statistical analysis was performed using paired t-test for comparisons within groups. MRI data were analyzed using repeated measure two-way analyses of variance (ANOVA). Statistical significance was established at  $p < 0.05$ .

## Supplementary Material

Refer to Web version on PubMed Central for supplementary material.

## Acknowledgment

We thank Prof. L. James Lee and his research group, in particular Yicheng Mao (Ohio State University), for their help in performing cryo-TEM analysis. We also thank Prof. Richard Bardbury (Ohio State University), for his invaluable technical advice and assistance with intravital microscopy imaging.

### Funding sources

This work was supported in part by National Heart, Lung, and Blood Institute Grant R21 HL106487 to SR and American Heart Association NCRP Scientist Development Grant 13SDG14500015 to AM. JAD was supported by NIDDK grant 5K01 DK099475.

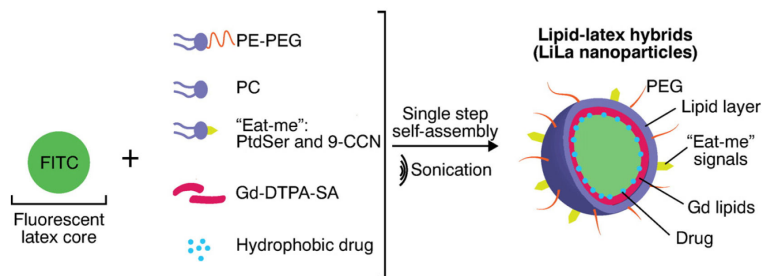
## References

- [1]. Qian BZ, Pollard JW. Macrophage diversity enhances tumor progression and metastasis. *Cell*. 2010; 141:39–51. [PubMed: 20371344]
- [2]. Rocha VZ, Libby P. Obesity, inflammation, and atherosclerosis. *Nat. Rev. Cardiol.* 2009; 6:399–409. [PubMed: 19399028]
- [3]. Sinclair H, Bourantas C, Bagnall A, Mintz GS, Kunadian V. OCT for the identification of vulnerable plaque in acute coronary syndrome. *JACC Cardiovasc. Imaging*. 2015; 8:198–209. [PubMed: 25677892]
- [4]. Weissleder R, Nahrendorf M, Pittet MJ. Imaging macrophages with nanoparticles. *Nat. Mater.* 2014; 13:125–138. [PubMed: 24452356]
- [5]. Siegwart DJ, Whitehead KA, Nuhn L, Sahay G, Cheng H, Jiang S, Ma ML, Lytton-Jean A, Vegas A, Fenton P, Levins CG, Love KT, Lee H, Cortez C, Collins SP, Li YF, Jang J, Querbes W, Zurenko C, Novobrantseva T, Langer R, Anderson DG. Combinatorial synthesis of chemically diverse core–shell nanoparticles for intracellular delivery. *Proc. Natl. Acad. Sci. U. S. A.* 2011; 108:12996–13001. [PubMed: 21784981]
- [6]. Kosuge H, Sherlock SP, Kitagawa T, Dash R, Robinson JT, Dai H, McConnell MV. Near infrared imaging and photothermal ablation of vascular inflammation using single-walled carbon nanotubes. *J. Am. Heart Assoc.* 2012; 1:e002568. [PubMed: 23316318]
- [7]. Mulder WJ, Jaffer FA, Fayad ZA, Nahrendorf M. Imaging and nanomedicine in inflammatory atherosclerosis. *Sci. Transl. Med.* 2014; 6(239):sr231.
- [8]. Maiseyeu A, Mihai G, Roy S, Kherada N, Simonetti OP, Sen CK, Sun Q, Parthasarathy S, Rajagopalan S. Detection of macrophages via paramagnetic vesicles incorporating oxidatively tailored cholesterol ester: an approach for atherosclerosis imaging. *Nanomedicine (Lond.)*. 2010; 5:1341–1356. [PubMed: 21128718]
- [9]. Maiseyeu A, Mihai G, Kampfrath T, Simonetti OP, Sen CK, Roy S, Rajagopalan S, Parthasarathy S. Gadolinium-containing phosphatidylserine liposomes for molecular imaging of atherosclerosis. *J. Lipid Res.* 2009; 50:2157–2163. [PubMed: 19017616]
- [10]. Maiseyeu A, Badgeley MA, Kampfrath T, Mihai G, Deiuliis JA, Liu C, Sun Q, Parthasarathy S, Simon DI, Croce K, Rajagopalan S. In vivo targeting of inflammation-associated myeloid-related protein 8/14 via gadolinium immunonanoparticles. *Arterioscler. Thromb. Vasc. Biol.* 2012; 32:962–970. [PubMed: 22308043]
- [11]. Champion JA, Mitragotri S. Role of target geometry in phagocytosis. *Proc. Natl. Acad. Sci. U. S. A.* 2006; 103:4930–4934. [PubMed: 16549762]
- [12]. Chambers E, Mitragotri S. Long circulating nanoparticles via adhesion on red blood cells: mechanism and extended circulation. *Exp. Biol. Med.* 2007; 232:958–966.
- [13]. Nance E, Zhang C, Shih TY, Xu Q, Schuster BS, Hanes J. Brain-penetrating nanoparticles improve paclitaxel efficacy in malignant glioma following local administration. *ACS Nano*. 2014; 8:10655–10664. [PubMed: 25259648]
- [14]. Yoon J, Jo W, Jeong D, Kim J, Jeong H, Park J. Generation of nanovesicles with sliced cellular membrane fragments for exogenous material delivery. *Biomaterials*. 2015; 59:12–20. [PubMed: 25941997]
- [15]. Muro S, Cui X, Gajewski C, Murciano JC, Muzykantov VR, Koval M. Slow intracellular trafficking of catalase nanoparticles targeted to ICAM-1 protects endothelial cells from oxidative stress. *Am. J. Physiol. Cell Physiol.* 2003; 285:C1339–C1347. [PubMed: 12878488]
- [16]. Muro S, Gajewski C, Koval M, Muzykantov VR. ICAM-1 recycling in endothelial cells: a novel pathway for sustained intracellular delivery and prolonged effects of drugs. *Blood*. 2005; 105:650–658. [PubMed: 15367437]
- [17]. Tacke F, Alvarez D, Kaplan TJ, Jakubzick C, Spanbroek R, Llodra J, Garin A, Liu JH, Mack M, van Rooijen N, Lira SA, Habenicht AJ, Randolph GJ. Monocyte subsets differentially employ CCR2, CCR5, and CX3CR1 to accumulate within atherosclerotic plaques. *J. Clin. Invest.* 2007; 117:185–194. [PubMed: 17200718]

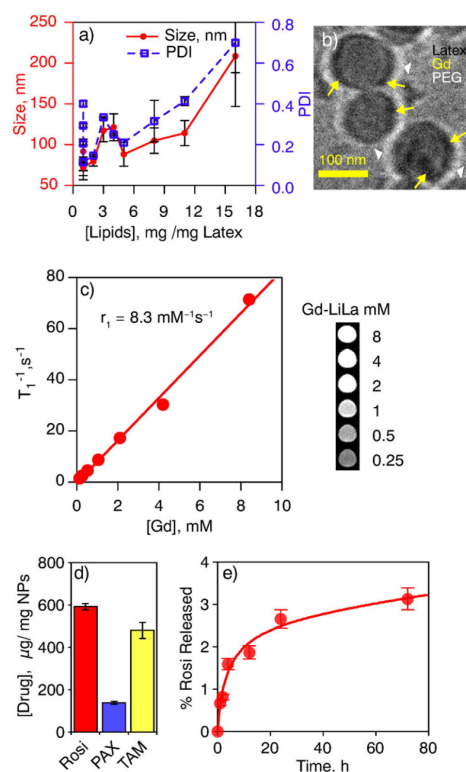
- [18]. Jakubzick C, Helft J, Kaplan TJ, Randolph GJ. Optimization of methods to study pulmonary dendritic cell migration reveals distinct capacities of DC subsets to acquire soluble versus particulate antigen. *J. Immunol. Methods*. 2008; 337:121–131. [PubMed: 18662693]
- [19]. Poon IKH, Lucas CD, Rossi AG, Ravichandran KS. Apoptotic cell clearance: basic biology and therapeutic potential. *Nat. Rev. Immunol.* 2014; 14:166–180. [PubMed: 24481336]
- [20]. Zhou Z, Lu ZR. Gadolinium-based contrast agents for magnetic resonance cancer imaging. *Wiley Interdiscip. Rev. Nanomed. Nanobiotechnol.* 2013; 5:1–18. [PubMed: 23047730]
- [21]. Zajac E, Schweighofer B, Kupriyanova TA, Juncker-Jensen A, Minder P, Quigley JP, Deryugina EI. Angiogenic capacity of M1- and M2-polarized macrophages is determined by the levels of TIMP-1 complexed with their secreted proMMP-9. *Blood*. 2013; 122:4054–4067. [PubMed: 24174628]
- [22]. Botelho RJ, Tapper H, Furuya W, Mojdami D, Grinstein S. Fc gamma R-mediated phagocytosis stimulates localized pinocytosis in human neutrophils. *J. Immunol.* 2002; 169:4423–4429. [PubMed: 12370376]
- [23]. Moore KJ, Sheedy FJ, Fisher EA. Macrophages in atherosclerosis: a dynamic balance. *Nat. Rev. Immunol.* 2013; 13:709–721. [PubMed: 23995626]
- [24]. Cheng Z, Tsourkas A. Monitoring phospholipase A<sub>2</sub> activity with Gd-encapsulated phospholipid liposomes. *Sci. Rep.* 2014; 4:6958. [PubMed: 25376186]
- [25]. Lin WW, Chen BC. Induction of cyclo-oxygenase-2 expression by methyl arachidonyl fluorophosphonate in murine J774 macrophages: roles of protein kinase C, ERKs and p38 MAPK. *Br. J. Pharmacol.* 1999; 126:1419–1425. [PubMed: 10217536]
- [26]. Hachet-Haas M, Converset N, Marchal O, Matthes H, Gioria S, Galzi JL, Lecat S. FRET and colocalization analyzer—a method to validate measurements of sensitized emission FRET acquired by confocal microscopy and available as an ImageJ Plug-in. *Microsc. Res. Tech.* 2006; 69:941–956. [PubMed: 17080432]
- [27]. Gerber D, Shai Y. Insertion and organization within membranes of the delta-endotoxin pore-forming domain, helix 4-loop-helix 5, and inhibition of its activity by a mutant helix 4 peptide. *J. Biol. Chem.* 2000; 275:23602–23607. [PubMed: 10811807]
- [28]. Austin CD, Wen X, Gazzard L, Nelson C, Scheller RH, Scales SJ. Oxidizing potential of endosomes and lysosomes limits intracellular cleavage of disulfide-based antibody-drug conjugates. *Proc. Natl. Acad. Sci. U. S. A.* 2005; 102:17987–17992. [PubMed: 16322102]
- [29]. Qiu QS, Fratti RA. The Na<sup>+</sup>/H<sup>+</sup> exchanger Nhx1p regulates the initiation of *Saccharomyces cerevisiae* vacuole fusion. *J. Cell Sci.* 2010; 123:3266–3275. [PubMed: 20826459]
- [30]. Alexis F, Pridgen E, Molnar LK, Farokhzad OC. Factors affecting the clearance and biodistribution of polymeric nanoparticles. *Mol. Pharm.* 2008; 5:505–515. [PubMed: 18672949]
- [31]. Kampfrath T, Deuliis JA, Moffatt-Bruce SD, Anderson J, Sun Q, Wood K, Ostrowski MC, Rajagopalan S. A mouse model of yellow fluorescent protein (YFP) expression in hematopoietic cells to assess leukocyte–endothelial interactions in the microcirculation. *Microvasc. Res.* 2009; 78:294–300. [PubMed: 19682464]
- [32]. Petros RA, DeSimone JM. Strategies in the design of nanoparticles for therapeutic applications. *Nat. Rev. Drug Discov.* 2010; 9:615–627. [PubMed: 20616808]
- [33]. Caravan P. Strategies for increasing the sensitivity of gadolinium based MRI contrast agents. *Chem. Soc. Rev.* 2006; 35:512–523. [PubMed: 16729145]
- [34]. Cavalieri F, Chiessi E, Villa R, Vigano L, Zaffaroni N, Telling MF, Paradossi G. Novel PVA-based hydrogel microparticles for doxorubicin delivery. *Biomacromolecules.* 2008; 9:1967–1973. [PubMed: 18533701]
- [35]. Tian J, Stella VJ. Degradation of paclitaxel and related compounds in aqueous solutions II: nonpimerization degradation under neutral to basic pH conditions. *J. Pharm. Sci.* 2008; 97:3100–3108. [PubMed: 17963215]
- [36]. Chan JM, Zhang L, Yuet KP, Liao G, Rhee JW, Langer R, Farokhzad OC. PLGA-lecithin-PEG core-shell nanoparticles for controlled drug delivery. *Biomaterials.* 2009; 30:1627–1634. [PubMed: 19111339]

- [37]. Kim Y, Lee Chung B, Ma M, Mulder WJ, Fayad ZA, Farokhzad OC, Langer R. Mass production and size control of lipid-polymer hybrid nanoparticles through controlled microvortices. *Nano Lett.* 2012; 12:3587–3591. [PubMed: 22716029]
- [38]. Colombo S, Cun D, Remaut K, Bunker M, Zhang J, Martin-Bertelsen B, Yaghmur A, Braeckmans K, Nielsen HM, Foged C. Mechanistic profiling of the siRNA delivery dynamics of lipid-polymer hybrid nanoparticles. *J. Control. Release.* 2015; 201:22–31. [PubMed: 25540904]
- [39]. Ceriello A. Thiazolidinediones as anti-inflammatory and anti-atherogenic agents. *Diabetes Metab. Res. Rev.* 2008; 24:14–26. [PubMed: 17990280]
- [40]. Cohen D. Drug regulation rosiglitazone: what went wrong? *Br. Med. J.* 2010; 341
- [41]. Ballesteros I, Cuartero MI, Pradillo JM, de la Parra J, Perez-Ruiz A, Corbi A, Ricote M, Hamilton JA, Sobrado M, Vivancos J, Nombela F, Lizasoain I, Moro MA. Rosiglitazone-induced CD36 up-regulation resolves inflammation by PPAR gamma and 5-LO-dependent pathways. *J. Leukoc. Biol.* 2014; 95:587–598. [PubMed: 24338629]
- [42]. Jung UJ, Torrejon C, Chang CCL, Hamai H, Worgall TS, Deckelbaum RJ. Fatty acids regulate endothelial lipase and inflammatory markers in macrophages and in mouse aorta a role for PPAR gamma. *Arterioscler. Thromb. Vasc.* 2012; 32:2929–2937.
- [43]. Becker L, Gharib SA, Irwin AD, Wijsman E, Vaisar T, Oram JF, Heinecke JW. A macrophage sterol-responsive network linked to atherogenesis. *Cell Metab.* 2010; 11:125–135. [PubMed: 20142100]
- [44]. Zhang L, Chan JM, Gu FX, Rhee JW, Wang AZ, Radovic-Moreno AF, Alexis F, Langer R, Farokhzad OC. Self-assembled lipid-polymer hybrid nanoparticles: a robust drug delivery platform. *ACS Nano.* 2008; 2:1696–1702. [PubMed: 19206374]
- [45]. Curfs DM, Ghesquiere SA, Vergouwe MN, van der Made I, Gijbels MJ, Greaves DR, Verbeek JS, Hofker MH, de Winther MP. Macrophage secretory phospholipase A2 group X enhances anti-inflammatory responses, promotes lipid accumulation, and contributes to aberrant lung pathology. *J. Biol. Chem.* 2008; 283:21640–21648. [PubMed: 18511424]
- [46]. Goncalves I, Edsfeldt A, Ko NY, Grufman H, Berg K, Bjorkbacka H, Nitulescu M, Persson A, Nilsson M, Prehn C, Adamski J, Nilsson J. Evidence supporting a key role of Lp-PLA2-generated lysophosphatidylcholine in human atherosclerotic plaque inflammation. *Arterioscler. Thromb. Vasc. Biol.* 2012; 32:1505–1512. [PubMed: 22499993]
- [47]. Elinder LS, Dumitrescu A, Larsson P, Hedin U, Frostegard J, Claesson HE. Expression of phospholipase A2 isoforms in human normal and atherosclerotic arterial wall. *Arterioscler. Thromb. Vasc. Biol.* 1997; 17:2257–2263. [PubMed: 9351398]
- [48]. Balboa MA, Perez R, Balsinde J. Amplification mechanisms of inflammation: paracrine stimulation of arachidonic acid mobilization by secreted phospholipase A2 is regulated by cytosolic phospholipase A2-derived hydroperoxyeicosatetraenoic acid. *J. Immunol.* 2003; 171:989–994. [PubMed: 12847271]
- [49]. Nagareddy PR, Murphy AJ, Storzaker RA, Hu Y, Yu S, Miller RG, Ramkhalawon B, Distel E, Westerterp M, Huang LS, Schmidt AM, Orchard TJ, Fisher EA, Tall AR, Goldberg IJ. Hyperglycemia promotes myelopoiesis and impairs the resolution of atherosclerosis. *Cell Metab.* 2013; 17:695–708. [PubMed: 23663738]
- [50]. Dutta P, Nahrendorf M. Regulation and consequences of monocytosis. *Immunol. Rev.* 2014; 262:167–178. [PubMed: 25319334]
- [51]. Heidt T, Sager HB, Courties G, Dutta P, Iwamoto Y, Zaltsman A, von Zur Muhlen C, Bode C, Fricchione GL, Denninger J, Lin CP, Vinegoni C, Libby P, Swirski FK, Weissleder R, Nahrendorf M. Chronic variable stress activates hematopoietic stem cells. *Nat. Med.* 2014; 20:754–758. [PubMed: 24952646]
- [52]. Schrijvers DM, De Meyer GR, Herman AG, Martinet W. Phagocytosis in atherosclerosis: molecular mechanisms and implications for plaque progression and stability. *Cardiovasc. Res.* 2007; 73:470–480. [PubMed: 17084825]
- [53]. Moore KJ, Tabas I. Macrophages in the pathogenesis of atherosclerosis. *Cell.* 2011; 145:341–355. [PubMed: 21529710]
- [54]. Getz GS, Reardon CA. Animal models of atherosclerosis. *Arterioscler. Thromb. Vasc. Biol.* 2012; 32:1104–1115. [PubMed: 22383700]

- [55]. Baitsch D, Bock HH, Engel T, Telgmann R, Muller-Tidow C, Varga G, Bot M, Herz J, Robenek H, von Eckardstein A, Nofer JR. Apolipoprotein E induces antiinflammatory phenotype in macrophages. *Arterioscler. Thromb. Vasc. Biol.* 2011; 31:1160–1168. [PubMed: 21350196]
- [56]. Wei J, Zheng M, Liang P, Wei Y, Yin X, Tang Y, Xue Y. Apolipoprotein E and its mimetic peptide suppress Th1 and Th17 responses in experimental autoimmune encephalomyelitis. *Neurobiol. Dis.* 2013; 56:59–65. [PubMed: 23619428]
- [57]. Richardson PD, Davies MJ, Born GV. Influence of plaque configuration and stress distribution on fissuring of coronary atherosclerotic plaques. *Lancet.* 1989; 2:941–944. [PubMed: 2571862]
- [58]. Mulder WJM, Strijkers GJ, van Tilborg GAF, Cormode DP, Fayad ZA, Nicolay K. Nanoparticulate assemblies of amphiphiles and diagnostically active materials for multimodality imaging. *Acc. Chem. Res.* 2009; 42:904–914. [PubMed: 19435319]
- [59]. Fink C, Goyen M, Lotz J. Magnetic resonance angiography with blood-pool contrast agents: future applications. *Eur. Radiol.* 2007; 17(Suppl. 2):B38–B44. [PubMed: 17650559]
- [60]. Weisberg SP, McCann D, Desai M, Rosenbaum M, Leibel RL, Ferrante AW. Obesity is associated with macrophage accumulation in adipose tissue. *J. Clin. Invest.* 2003; 112:1796–1808. [PubMed: 14679176]
- [61]. Lumeng CN, Bodzin JL, Saltiel AR. Obesity induces a phenotypic switch in adipose tissue macrophage polarization. *J. Clin. Invest.* 2007; 117:175–184. [PubMed: 17200717]
- [62]. Nishimura S, Manabe I, Nagasaki M, Seo K, Yamashita H, Hosoya Y, Ohsugi M, Tobe K, Kadowaki T, Nagai R, Sugiura S. In vivo imaging in mice reveals local cell dynamics and inflammation in obese adipose tissue. *J. Clin. Invest.* 2008; 118:710–721. [PubMed: 18202748]
- [63]. Mulder WJ, Strijkers GJ, Nicolay K, Griffioen AW. Quantum dots for multimodal molecular imaging of angiogenesis. *Angiogenesis.* 2010; 13:131–134. [PubMed: 20552267]
- [64]. Cheng ZL, Al Zaki A, Hui JZ, Muzykantov VR, Tsourkas A. Multifunctional nanoparticles: cost versus benefit of adding targeting and imaging capabilities. *Science.* 2012; 338:903–910. [PubMed: 23161990]



**Fig. 1.** Schematic illustration of components in LiLa nanoparticles. The single step self-assembly with a latex core template, lipids, dyes/drugs yields theranostic lipid–latex hybrid nanoparticles (LiLa). The targeting to macrophages is achieved by phagocytic signals phosphatidylserine (PtdSer) and cholesterol-9-carboxynonanoate (9-CCN). LiLa formulations bearing Gd or Alexa-647 imaging probes are expected to serve as contrast agents for MRI and fluorescence imaging.

**Fig. 2.**

Physicochemical, magnetic and drug-loading properties of LiLa. (a) A relationship between the concentration of the lipid fraction in LiLa, nanoparticles' size and dispersity. The hydrodynamic size and polydispersity index (PDI) was measured by DLS for 12 formulations and presented as mean of three replicates  $\pm$  standard error on double Y-axis (red, left is size and right, blue is PDI). (b) The cryo-TEM micrographs of Gd-LiLa nanoparticles. Yellow arrows indicate the electron-dense spots attributed to Gd deposition on the surface of the latex. White arrows depict prominent PEG corona around the particles. (c) MRI relaxivity characteristics of Gd-LiLa nanoparticles presented as a function of the relaxation times  $T_1$  vs gadolinium concentration.  $T_1$  values were extracted from the signal intensity of the corresponding phantoms (inset) after curve fitting using a range of repetition times (see methods). The molar relaxivity,  $r_1$ , was obtained from the slope of  $T_1^{-1}$  vs gadolinium concentration. (d) Drug loading capacity of LiLa as determined on three model hydrophobic drugs: rosiglitazone (Rosi), paclitaxel (PAX) and tamoxifen (TAM). The data obtained from three different formulations for each drug is presented as mean  $\pm$  standard error. (e) Plasma stability of Rosi-LiLa as determined by dynamic dialysis against 50% human plasma at 37 °C.

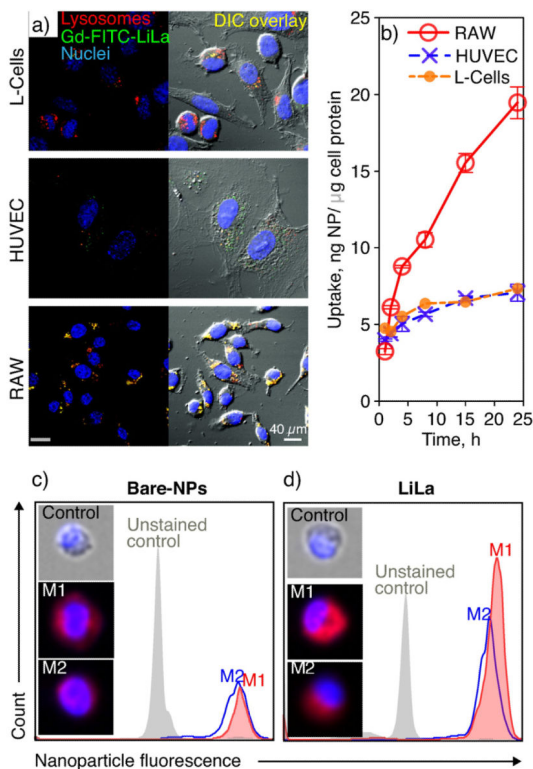


**Fig. 3.** In vitro characterization of various LiLa nanoparticles in different cell lines. (a) Confocal microscopy was used to evaluate Gd-FITC-LiLa (green) uptake in fibroblasts (L-cells), human umbilical vein endothelial cells (HUVEC) and macrophages (RAW 264.7). The right panel represents the overlay of fluorescent and bright field (DIC) micrographs. For visualization of the lysosomal compartment, cells were stained with antibody against lysosomal-associated membrane protein 1 (red). (b) Time-dependent uptake of Gd-LiLa by different cell lines. The data were normalized to the protein content in cell lysates. The quantification was based on 3–4 independent replicates, and the error bars represent standard deviation. The statistical analysis of the time-course trend by two-way ANOVA demonstrated a significant difference in uptake of Gd-LiLa by RAW cells as compared to HUVEC ( $p < 0.001$ ) and L-cells ( $p < 0.01$ ). (c,d) Flow cytometry analysis of bone marrow derived macrophages that were polarized to M1 and M2 phenotypes and treated with bare latex or LiLa nanoparticles. The M1 inflammatory phenotype showed higher uptake of LiLa particles compared to M2 phenotype. Single-cell analysis by means of imaging flow-cytometry (inset) suggested intracellular localization of LiLa in M1-macrophages (see text).



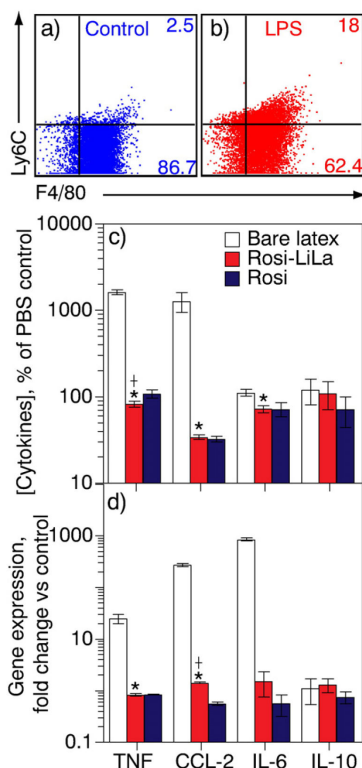


**Fig. 4.** Therapeutic properties of rosiglitazone-loaded LiLa (Rosi-LiLa) in an in vitro model of inflammation. (a, b) An in vitro model of inflammation was created and evaluated by flow-cytometry using a marker of inflammation lymphocyte antigen 6C (Ly6C) and a macrophage-specific antibody F4/80. A treatment of RAW 264.7 macrophages with lipopolysaccharide (LPS) gave rise to inflammatory macrophages, of which 18% were Ly6C-positive. The control macrophages (buffer-treated) were only 2.5%-positive for Ly6C. (c, d) Antiinflammatory effects of Rosi-LiLa were studied in the inflammation model described above. A treatment of inflammatory macrophages with Rosi-LiLa resulted in significant reduction of Th1 response with significantly attenuated production of indicated cytokines (c) and mRNA transcripts (d). The data are expressed on a logarithmic scale as percent change in cytokine concentration over concentration in cells treated with phosphate buffered saline (PBS). The error bars denote standard deviation of three separate experiments performed in triplicate. t-Test was used to determine significance. \*p < 0.05, †p < 0.01 vs. PBS control.

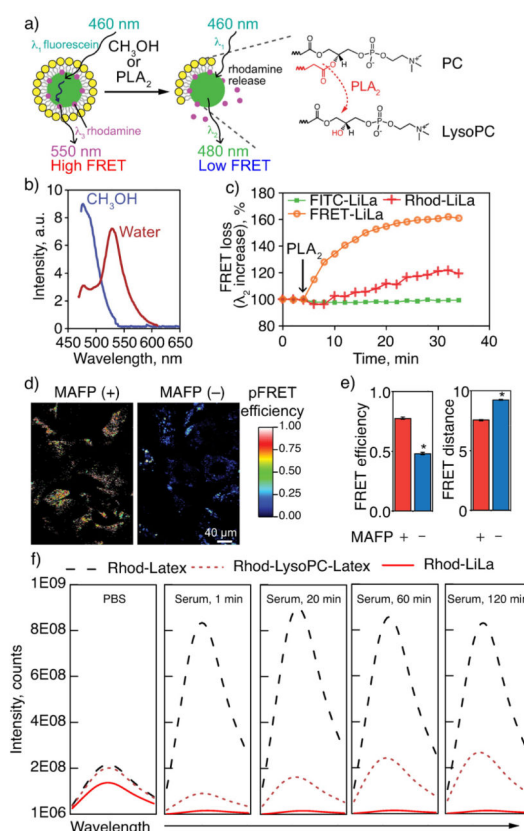


**Fig. 5.**

Controlled release of the model drug from LiLa nanoparticles. (a) Design of FRET-LiLa beacon: fluorescein incorporated latex core (green) is decorated with rhodamine (red) producing a FRET pair with excitation  $\lambda_1 = 460$  nm and emission  $\lambda_3 = 550$  nm. Upon cleavage of phospholipid layer (yellow) with methanol or phospholipase PLA<sub>2</sub>, rhodamine is released resulting in a FRET loss (fluorescein emitting at  $\lambda_2 = 480$  nm). Inset: schematic representation of formation of LysoPC, the product of PLA<sub>2</sub>-induced phospholipid hydrolysis. (b) Fluorescence emission spectra of FRET-LiLa in water (red curve) and methanol (blue curve). (c) FRET-loss was monitored by recording changes in  $\lambda_2$  (480 nm) signal in three LiLa formulations after exposure to PLA<sub>2</sub>. Snake-venom PLA<sub>2</sub> was simultaneously added to all three formulations at 6 min of incubation. (d) Confocal fluorescence images of FRET-LiLa-treated RAW cells in sensitized emission FRET (pFRET) mode before (MAFP-) and after (MAFP+) the treatment with PLA<sub>2</sub> inhibitor (MAFP). (e) pFRET image analysis (7–10 slides per group were analyzed) gave rise to FRET efficiency and FRET distance of MAFP treated and untreated cells. A distance 10 nm indicates no FRET. (f) Rhodamine fluorescence emission spectra recorded in PBS or 30% human serum over time for latex nanoparticles incorporating rhodamine but no phospholipids (Rhod-Latex), LiLa particles with rhodamine and phospholipids (Rhod-LiLa), and LiLa particles with rhodamine where 50% of phosphatidylcholine was replaced with Lyso-phosphatidylcholine (Rhod-LysoPC-Latex). t-Test was used to determine significance. \* $p < 0.05$ .

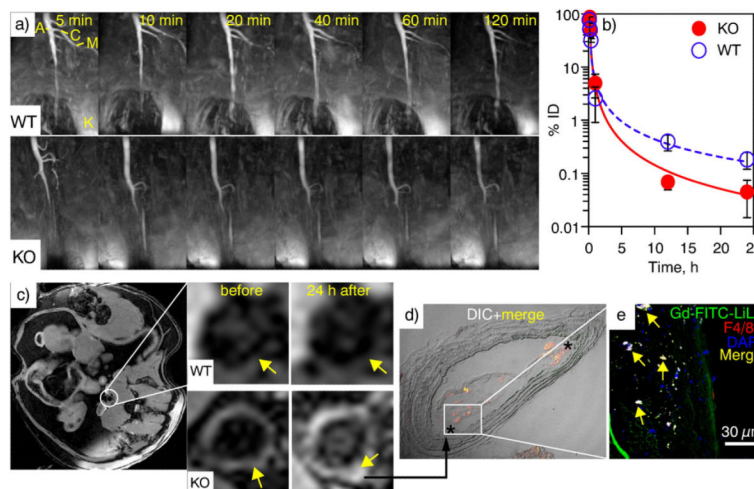


**Fig. 6.** In vivo MRI, blood clearance and macrophage targeting characteristics of Gd-FITC-LiLa nanoparticles. (a) Representative time-lapse magnetic resonance imaging (MRI) scans of vasculature in wild type (WT) and atherosclerotic ApoE<sup>-/-</sup> knockout (KO) animals following injection of Gd-FITC-LiLa. The early time-point images show high contrast enhancement in abdominal aorta (A), celiac trunk (C), superior mesenteric artery (M), and kidney (K). (b) The Gd-FITC-LiLa blood clearance in WT and KO mice was determined by measuring the concentration of Gd in blood over time by inductively coupled plasma mass spectrometry. The data presented are from seven mice (n = 4 KO and n = 3 WT) and the error represents the standard deviation of biological replicates. (c) A representative T<sub>1</sub>-weighted gradient echo MR scan in the axial plane (right) and the corresponding magnifications depicting the aortic wall (arrows) in WT and KO mice before and 24 h after Gd-FITC-LiLa injection. Prominent contrast-enhanced delineation of the aortic wall is clearly seen as bright hyperintense signal in KO mice 24 h post Gd-FITC-LiLa injection. (d, e) Confocal microscopy micrographs of atherosclerotic plaque of KO mice treated with Gd-FITC-LiLa. (d) The accumulation of Gd-FITC-LiLa in shoulders of atherosclerotic plaque (asterisks) was observed in overlaid DIC and fluorescence images at 20× magnification. (e). The signal from F4/80-positive (red) macrophages co-localized with fluorescence of Gd-FITC-LiLa (green) and was seen as yellow on micrographs of atherosclerotic plaque at 60× magnification. Nuclei (blue) were detected through staining with DAPI.

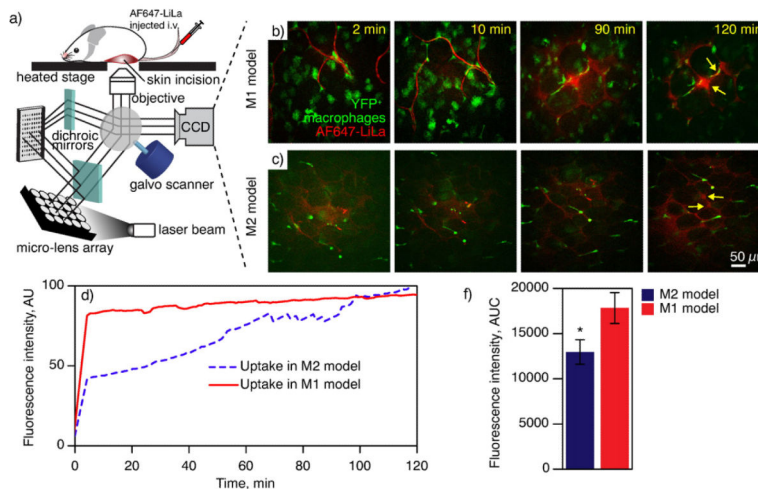


**Fig. 7.** In vivo confocal imaging with LiLa nanoparticles. (a) Schematic view of a confocal microscope used for intravital imaging of adipose. A laser light is focused through a pinhole array, and then reflected into a galvanometer scanner (galvo) by the dichroic mirror. The laser beam is then used to scan the sample through galvanometer as it moves across the image. The emitted light is then “descanned” back to the galvanometer allowing for synchronized imaging with minimal distortion. A live imaging is performed through a small incision in animal's adipose pad. (b, c) Representative time-lapse confocal images of the adipose tissue in M1 and M2 mouse models of adipose inflammation. “M1” (obese, n = 3) and “M2” (lean, n = 3) yellow fluorescent protein (YFP) reporter mice were injected with AF647-LiLa nanoparticles and subjected to intravital imaging monitoring fluorescence signals from YFP<sup>+</sup> macrophages (green) and AF647-LiLa (red) over time. (d) Quantification of mean fluorescence intensity of AF647 (expressed as % of maximum fluorescence) in YFP<sup>+</sup> macrophages over time. Image series were analyzed with ImageJ software by selecting YFP<sup>+</sup> region of interest in each frame, followed by analysis of average fluorescence intensity of AF647 for each time point (e) Area under the curve (AUC) was calculated to determine the rate of uptake of AF647-LiLa in macrophages. t-Test \*p < 0.01 M1-model vs M2-model.

**Table 1**Particle size of Gd-Lila formulation.<sup>a</sup>

Sample	Water		PBS buffer		10% human serum	
	Diameter (nm)	PDI	Diameter (nm)	PDI	Diameter (nm)	PDI
Gd-LiLa(0.16 h)	51.28 ± 0.46	0.05	86.50 ± 3.56	0.2	98.99 ± 4.57	0.39
Gd-LiLa (48 h)	53.92 ± 0.23	0.07	49.69 ± 0.41	0.05	75.32 ± 5.15	0.41
Bare-latex(0.16 h)	54.49 ± 0.57	0.07	45.36 ± 0.24	0.07	397.40 ± 215.59	0.84
Bare-latex(48 h)	91.56 ± 0.47	0.23	51.00 ± 1.86	0.13	693.40 ± 416.96	0.49

<sup>a</sup>Data as mean ± standard deviation (n= 3). Samples in PBS buffer and 10% human serum were incubated at 37 °C.